High-Capacity Zinc Anode Enabled by a Recyclable Biomass Bamboo Membrane Separator

Jianfeng Ma, Xin Shi, Zhihui Wang, Lijun Zhou, Xinge Liu, Xihong Lu,* and Zehui Jiang**

Aqueous zinc ion batteries have gained attention as viable energy storage systems, yet the occurrence of detrimental side reactions and Zn dendrite formation undermines the efficiency of Zn anodes. Controlling water activity have proven to be an effective strategy in mitigating these challenges. However, strategies such as electrolyte design and electrode protection layer show weakness to varying degrees. Here, a new oxygen-functionalized biomass bamboo membrane separator (denoted as BM) is proposed to restrain the activity of water molecules. This BM separator features a unique, multi-tiered 2D interlayer that facilitates rapid ion diffusion. Additionally, the oxygen functional groups of the BM separator can form hydrogen bonds with water molecules, effectively transforming water molecules from a free state to a bound state. Consequently, the Zn/Zn asymmetric coin cell using BM can work at the ultrahigh rate and capacity of 30 mA cm^{-2} and 30 mAh cm^{-2} for more than 80 h while its counterparts using glass fiber can barely work. Moreover, full cells using BM separator exhibited a capacity retention of 89.7% after 1000 cycles at 10 A g^{-1}. This study reveals the important influence of water-limited activity on Zn anode protection and provides an avenue for the design of novel separator.

1. Introduction

Benefitted from the intrinsic merits of Zn anode such as high theoretical capacity (820 mAh g^{-1}) and suitable potential (−0.76 V vs standard hydrogen electrode (SHE)), aqueous Zn ion batteries (AZIBs) are finding their place in large-scale energy storage system where safety, cost, scalability, and carbon footprint matter most.[1–8] However, the poor cycling stability, originated from the notorious dendrite growth and side reaction of the Zn anode, hinders the practical application of AZIBs.[9–11] Theoretically, these issues are highly connected to the activity of water molecules.[12,13] In conventional concentrated electrolyte, Zn^{2+} are mainly solvated by H_2O molecules and form the primary solvation sheath of $[Zn(H_2O)_n]^{2+}$.[14] During the Zn deposition process, lots of active H_2O molecules are released and get in touch with Zn anode as the desolvation of $[Zn(H_2O)_n]^{2+}$ proceeds, triggering side reactions such as hydrogen evolution reaction (HER), passivation, etc.[15] The as-formed by-product further disturb the electric field distribution of the Zn anode, driving inhomogeneous Zn^{2+} flux and causing uneven Zn deposition.[16] Therefore, controlling the activity of water molecules is the key to suppress the dendrite growth and side reaction of Zn anode.

To tackle the issues caused by water molecules, electrolyte optimization and electrode modification strategies including surface layer protection have been proposed to stabilize Zn anode.[17–20] Concretely, Wang et al. reported a 1 m $Zn(TFSI)_2$ + 20 m LiTFSI (HCE) to astrict the content of solvated H_2O and endow Zn/O_2 battery with more than 200 cycles lifespan.[21] However, with the wide investigation of HCE, hesitations such as economic cost and environmental impact have arisen. Alternatively, the solvation structure of Zn^{2+} can be adjusted by introducing a functional co-solvent (i.e., dimethyl sulfoxide,[22] ethylene glycol,[23] and triethyl phosphate[24]). The newly recruited solvent molecules show a higher coordination tendency with Zn^{2+} and reduce the number of solvated water molecules. However, the exotic co-solvent is usually toxic and flammable, which is inconsistent with the environmental friendliness and safety characteristics of AZIBs. The activity of water molecules can also be inhibited to a certain extent by constructing a functional protective interface (i.e., Zeolitic Imidazolate Framework-7,[25] ZnF_2[26]) on the zinc anode. However, when the zinc anode is cycled under high area capacity and high depth of discharge (DOD), the serious volume change of zinc metal (1.7 µm mAh^{-1}) will lead to damage, cracking or even falling off of the modified interface, resulting in the decrease of stability. In addition, the complicated preparation process and high cost of the currently modified Zn anode makes it difficult to be produced and used in a large scale. Therefore, strategic minimization of the activity of water molecules

---

J. Ma, Z. Wang, X. Liu, Z. Jiang
Key Lab of Bamboo and Rattan Science & Technology
International Center for Bamboo and Rattan
Beijing 100102, P. R. China
E-mail: liuxinge@icbr.ac.cn; jiangzehui@icbr.ac.cn

X. Shi, L. Zhou, X. Lu
MOE of the Key Laboratory of Bioinorganic and Synthetic Chemistry
The Key Lab of Low-carbon Chem & Energy Conservation of Guangdong Province
School of Chemistry
Sun Yat-Sen University
Guangzhou 510275, P. R. China
E-mail: luxh6@mail.sysu.edu.cn

The ORCID identification number(s) for the author(s) of this article can be found under https://doi.org/10.1002/adma.202406429

DOI: 10.1002/adma.202406429

to construct Zn anode under high capacity still remains challenging.

As a crucial element within the battery, the separator significantly influences overall battery performance.[27] Presently, glass fiber (GF) separators are widely utilized, yet they exhibit several drawbacks. These disadvantages include mechanical fragility, susceptibility to crumbling, and the presence of large, irregularly sized pores, which collectively make them vulnerable to zinc dendrite formation and the puncturing of the GF separator.[28,29] Consequently, there remains a notable absence of a more effective separator solution capable of shielding the Zn anode from issues induced by water molecules. Herein, we reported a new biomass bamboo membrane (BM) separator with high recyclability to suppress the activity of water molecules in AZIBs. In contrast to the GF separator, this BM separator possesses a distinctive, multi-level 2D interlayer architecture, which allows rapid ion diffusion.[30] Moreover, by grafting oxygen functional groups to the BM separator, it is able to retain the activity of water molecules via the hydrogen bonding effect, altering the state of water molecules from free to bound. Consequently, the Zn/Zn symmetric coin cell using a BM separator can work at the ultrahigh rate and capacity of 30 mA cm^{-2} and 30 mAh cm^{-2} for more than 80 h with a near-unity coulombic efficiency of ≈99% while its counterparts using GF can barely work. Moreover, Zn/NVO full cell shows 89.7% capacity retention after 1000 cycles at 10 A g^{-1}, demonstrating the application potential of the biomass BM separator for AZIBs.

2. Results and Discussion

Biomass bamboo membranes have a wide range of sources, high renewability, environmental friendliness, and unique physicochemical properties that are very much in line with the environmentally friendly and sustainable characteristics of AZIBs. The high cellulose content and stable structure of bamboo membranes provide excellent mechanical strength and chemical stability, making them ideal raw materials for the separator of AZIBs. In addition, the short growth cycle of bamboo not only reduces dependence on forest resources but also lowers the carbon footprint, thus contributing to environmental protection and ecological balance while enhancing battery performance.

Figure S1 (Supporting Information) displays a slender and translucent membrane that has been carefully separated from the inner lining of natural bamboo stems. The preparation method of BM is shown in **Figure 1**a. The bamboos of a four-year-old bamboo are sawed and placed in the deionized water. The BM is taken off after it floats to the surface of the deionized water. The BM is prepared by immersing BM into 30% H_2O_2 solutions. Scanning electron microscopy (SEM) was employed to investigate the surface architecture of the BM. Contrary to the smooth appearance perceived by the naked eye, the surface of BM is characterized by a degree of roughness, alongside a series of linear openings dispersed randomly across the surface (Figure 1b). These openings act as conduits for the transmembrane transport of liquids and ions, facilitating ion diffusion perpendicular to the plane of the membrane. The chemical structures of GF and BM are investigated by Fourier transform infrared spectroscopy (FTIR) and Raman spectra. In FTIR spectra, the peaks at ≈1003 and 451 cm^{-1} are assigned to Si—O—Si and Si—O stretching vibration of GF. BM shows O-H stretching at ≈3296 cm^{-1}, while this is missing in GF. Other bands located at 2898, 1605, 1420, 1319, 1162, 1031, 893, 662, and 551 cm^{-1} are attributed to C–H stretching from $-CH_2-$, O–H bending, symmetric CH_2 bending, CH_2 rocking, anti-symmetrical bridge C–O–C stretching, C–O stretching, β-linkage of cellulose, OH out of plane bending, and C–C stretching, respectively.[28] Figure 1d shows the Raman spectra of GF and BM. Only one peak can be observed for GF, which is associated with the Si–O vibration. In contrast, multiple peaks can be found for BM, confirming its cellulose nature. Figure S2 (Supporting Information) shows the XRD pattern of BM. The peak located at 22.6° can be assigned to the characteristic peak of cellulose. Large tensile strength of 0.32 MPa can be achieved for BM, indicating its good mechanical properties (Figure 1e). Moreover, BM possesses significantly lower mass and thickness compared to GF, which can effectively decrease the mass of the full cell and the amount of electrolyte, thus improving the energy density of the full cell (Figure 1f–g).

To assess the interfacial interactions between BM and water molecules, FTIR spectroscopy was conducted on GF and BM with 1 м $Zn(OTf)_2$ solution content of 80%. It's identified that the peaks at ≈3240, 3430, and 3600 cm^{-1} are indicative of strong, medium, and weak hydrogen bonding (HB) stretching vibrations (**Figure 2**a). Notably, the O–H stretching vibrations of BM shows a negative shift compared to that of GF, suggesting that BM possesses a superior capability for water molecule binding. Moreover, BM also shows enhanced interaction with OTf^- anion in the electrolyte. As shown in Figure 2b, the peaks located at ≈1027 cm^{-1} can be ascribed to the free OTf^- anions in different solutions while the peak ranges from 1045 to 1065 cm^{-1} could be assigned to the coordinated OTf^- anions.[11] For BM, a negative shift of peak at ≈1026 cm^{-1} and the occurrence of a broad peak can be identified, indicating the interaction between OTf^- and BM is formed. A similar phenomenon is also verified by the vibrations of $-CF_3$ and $-SO_3$ (Figure 2c). Compared to GF, the peak representing C-F shows a negatively shift while the S=O signal can be observed, suggesting the coordination environment between OTf^- and BM. Such solvation structure variations of Zn^{2+} are also testified in Raman spectra (Figure S3, Supporting Information). Differential scanning calorimetry (DSC) was also conducted to investigate the bonding condition between water molecules and BM. As shown in Figure S4 (Supporting Information), the freezing point of electrolytes on BM is significantly decreased, indicating the strong interfacial water bonding capability.

The binding energies between BM and GF with water were analyzed using molecular dynamics (MD) simulations, corroborating that BM exhibits robust interactions with water molecules. As shown in Figure 2d,e and Figure S5 (Supporting Information), the density and energy of hydrogen bonds at the interface between BM and water molecules surpass those observed between GF and water molecules. This result highlights a pronounced interfacial affinity of BM toward water molecules. Moreover, BM also shows an enhanced binding tendency with OTf^- than that of GF, in well agreement with the experimental results. Density functional theory (DFT) calculation also proves the enhanced interaction between BM and water molecules, as indicated by the lower binding energy of GF and BM with water molecules in Figure 2f, Figures S6 and S7 (Supporting Information). The

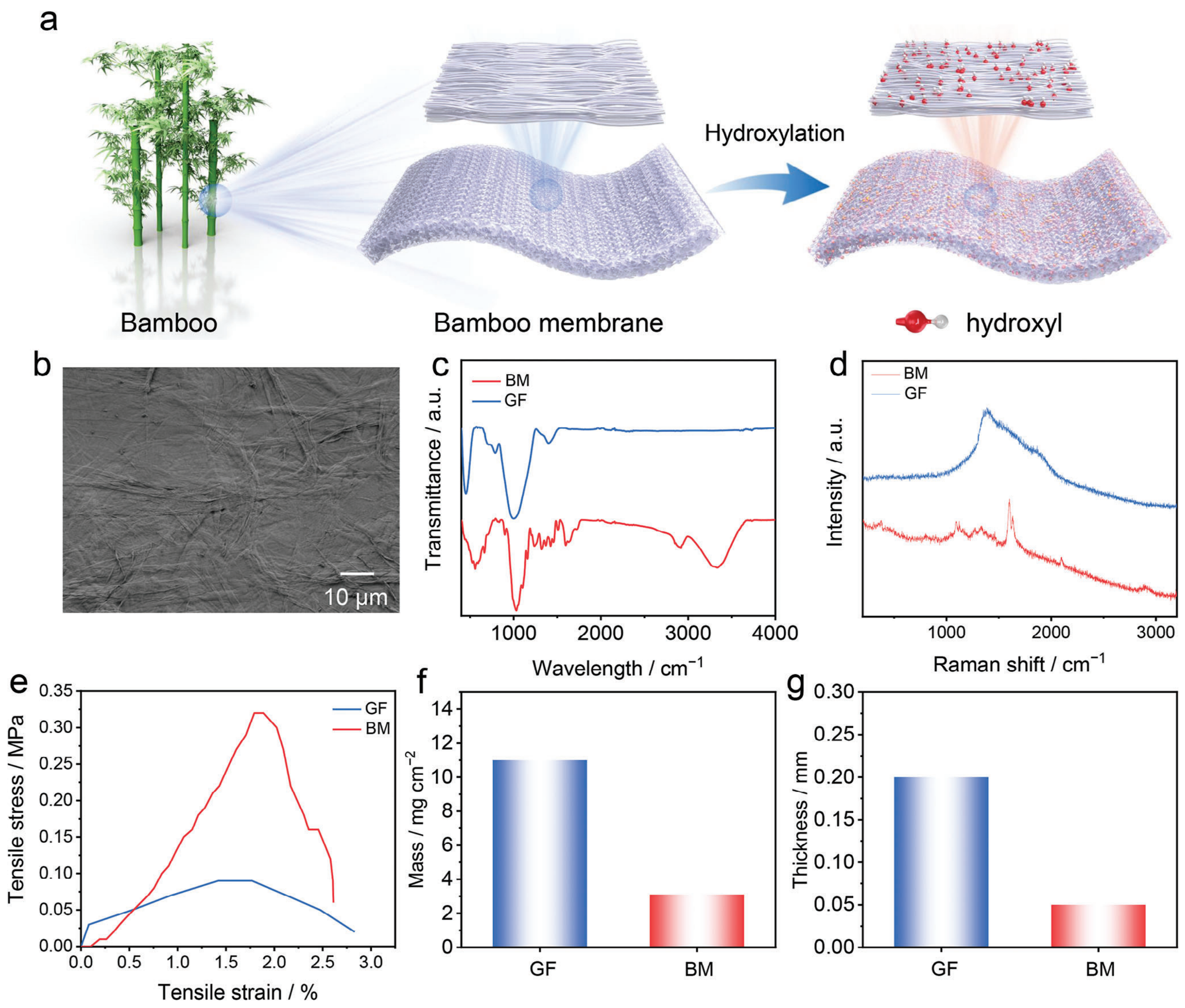

Figure 1. a) Schematic illustration of the preparation process for BM. b) SEM image of BM. c) FTIR spectra, d) Raman spectra, and e) tensile σ-ε curves of GF and BM separators. Comparison of f) mass and g) thickness between GF and BM.

binding energy between BM and OTf$^-$ (−0.8 eV) is lower than that of GF and OTf$^-$ (−0.62 eV), suggesting the interaction between BM and OTf$^-$ is also increased. In addition, the calculated Zn^{2+} transference number (t_+) of Zn/Zn cells using the BM separator (0.49) is higher than using the GF separator (0.22), indicating BM is more favorable for Zn^{2+} migration, which may be due to its stronger interaction with anions (Figure S8, Supporting Information). More importantly, a microzone model was used to emulate the electrical and concentration gradients within a Zn/Zn symmetric cell. Figure 2g–j depict the electric fields and Zn^{2+} ion concentration gradients for BM and GF separators at a current density of 5 mA cm^{-2}. Based on the Nernst-Planck equation, using GF as the separator results in a significant "tip effect" on the Zn surface, indicated by an uneven distribution and concentration of the electric field (Figure 2g).[31] In contrast, when BM is employed as the separator, the electrostatic interaction between BM and Zn^{2+} ions yield a uniform distribution of the electric field across the surface of the dendritic crystal and a similarly even concentration gradient on the zinc surface (Figure 2h). Furthermore, the vicinity of the electrode surface exhibits a higher Zn^{2+} concentration than that observed with GF, diminishing concentration polarization in the Zn/Zn symmetric cell (Figure 2i,j). The current density field from GF and BM is illustrated in Figure S9 (Supporting Information). GF shows uneven current density distribution, due to the inhomogeneous concentration gradient. In contrast, BM exhibits a homogeneous current density distribution.

The electrochemical stability windows of Zn/Ti cells using GF and BM were evaluated. As depicted in Figure S10 (Supporting Information), a wider working window of BM is observed, where both cathodic and anodic limits are expanded, which may be due to that BM suppresses the activity of H_2O. The desolvation of Zn^{2+} is an important process during Zn plating, which can significantly influence the of morphology Zn deposits. Figure S11

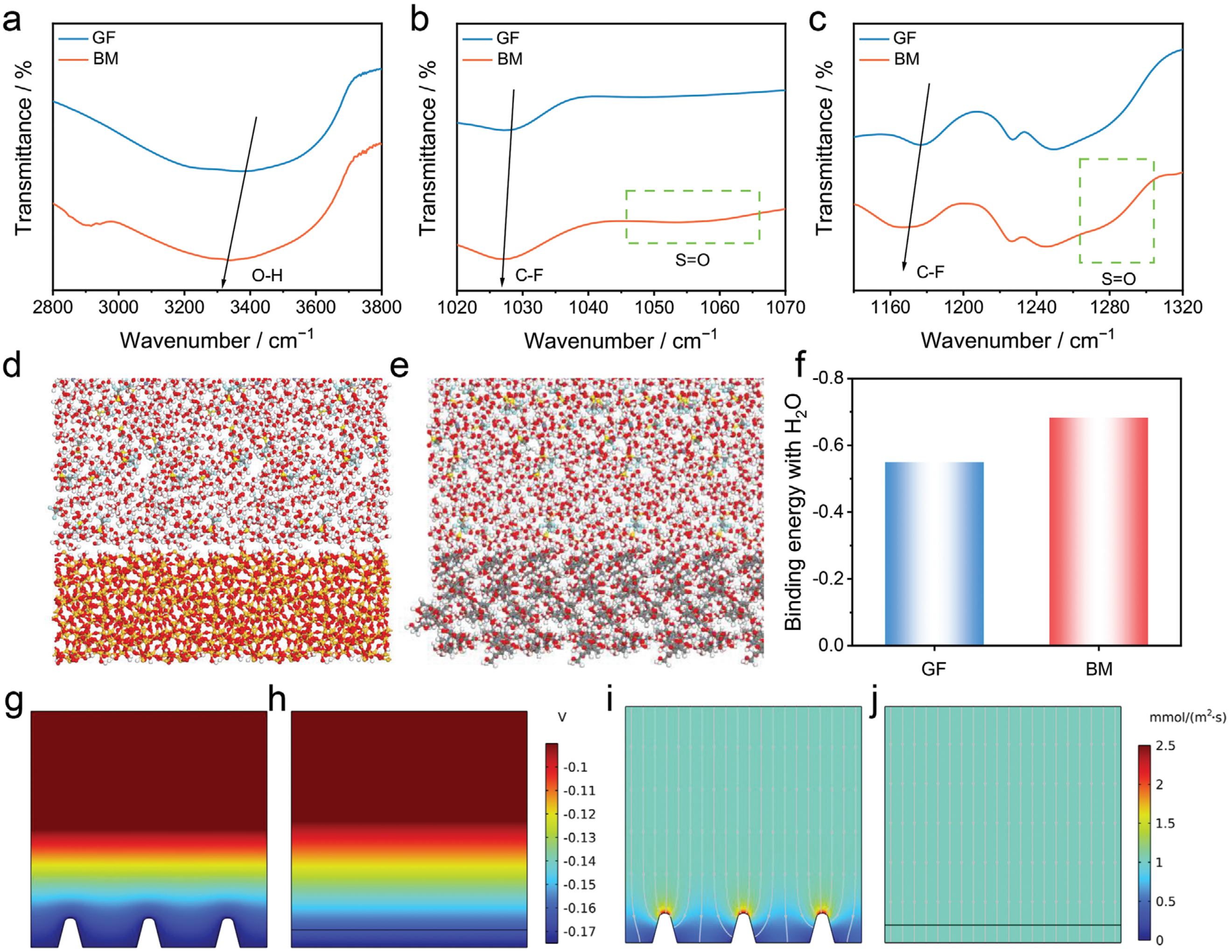

Figure 2. a–c) FTIR spectra of GF and BM with 80 wt% 1 M $Zn(OTf)_2$ solution. d) 3D snapshot of MD calculation for the interaction between GF and 1 M $Zn(OTf)_2$ solution. e) 3D snapshot of MD calculation for the interaction between BM and 1 M $Zn(OTf)_2$ solution (H, white; C, grey; O, red; F, cyan; S, yellow; Si, orange). f) Binding energy comparison between GF-H_2O and BM-H_2O. The electrical field models are based on g) GF and h) BM. The zinc ion concentration field models are based on i) GF and j) BM.

(Supporting Information) shows the calculated activation energy (E_a) of Zn^{2+} desolvation based on the Arrhenius equation.[32] The E_a of GF and BM separators are 52.6, and 42.5 kJ mol^{-1}, manifesting the lower energy barrier for Zn^{2+} desolvation with BM. Exchange current is used to evaluate Zn deposition kinetics Compared to GF separators, a promoted exchange current was observed for BM separators, from 1.7 to 2.4 mA cm^{-2} (Figure S12, Supporting Information), indicating the facilitated Zn deposition kinetics.[33] Chronoamperometry (CA) measurement is carried out to investigate the difference of Zn diffusion behavior using GF and BM separators (Figure S13, Supporting Information). At a constant voltage of −150 mV, Zn shows a persistent 2D diffusion with GF while 3D diffusion (on the basis of a nearly unchanged current curve after 10 s is observed with BM, indicating the more homogeneous nucleation of Zn with BM separators, which is beneficial for the suppression of dendrite growth.

To investigate the impact of BM on the reversibility of Zn plating/striping, Zn/Cu asymmetric cells using GF and BM were assembled and tested at 1 and 1 mA cm^{-2}. The coulombic efficiency (CE) values of Zn/Cu cells are illustrated in **Figure** 3a. With a BM separator, the cell achieves an average CE of 99% across all 300 cycles. However, employing the GF separator results in a reduced average CE during the initial few cycles; thereafter, the CE fluctuates dramatically. This fluctuation is attributed to the formation of zinc dendrites and penetration through the separator. As depicted in Figure 3b,c, the galvanostatic charge-discharge (GCD) curves of Zn/Cu cells equipped with BM separator at the 5th, 150th, and 300th cycles align perfectly, showing a minimal charge-discharge voltage disparity of 75 mV, which signifies outstanding reversibility. Conversely, the alignment of GCD curves is less precise when utilizing the GF separator. As shown in Figure 3d, a poor stability (≈61 h) with low coulombic efficiency (CE) is acquired with GF at 1 mA cm^{-2} and 1 mAh cm^{-2}. On the contrary, the Zn/Zn cell with BM exihibits a prolonged lifespan (≈1000 h) with a high CE. Such boosted performance should be related to the elimited side reactions and dendrite

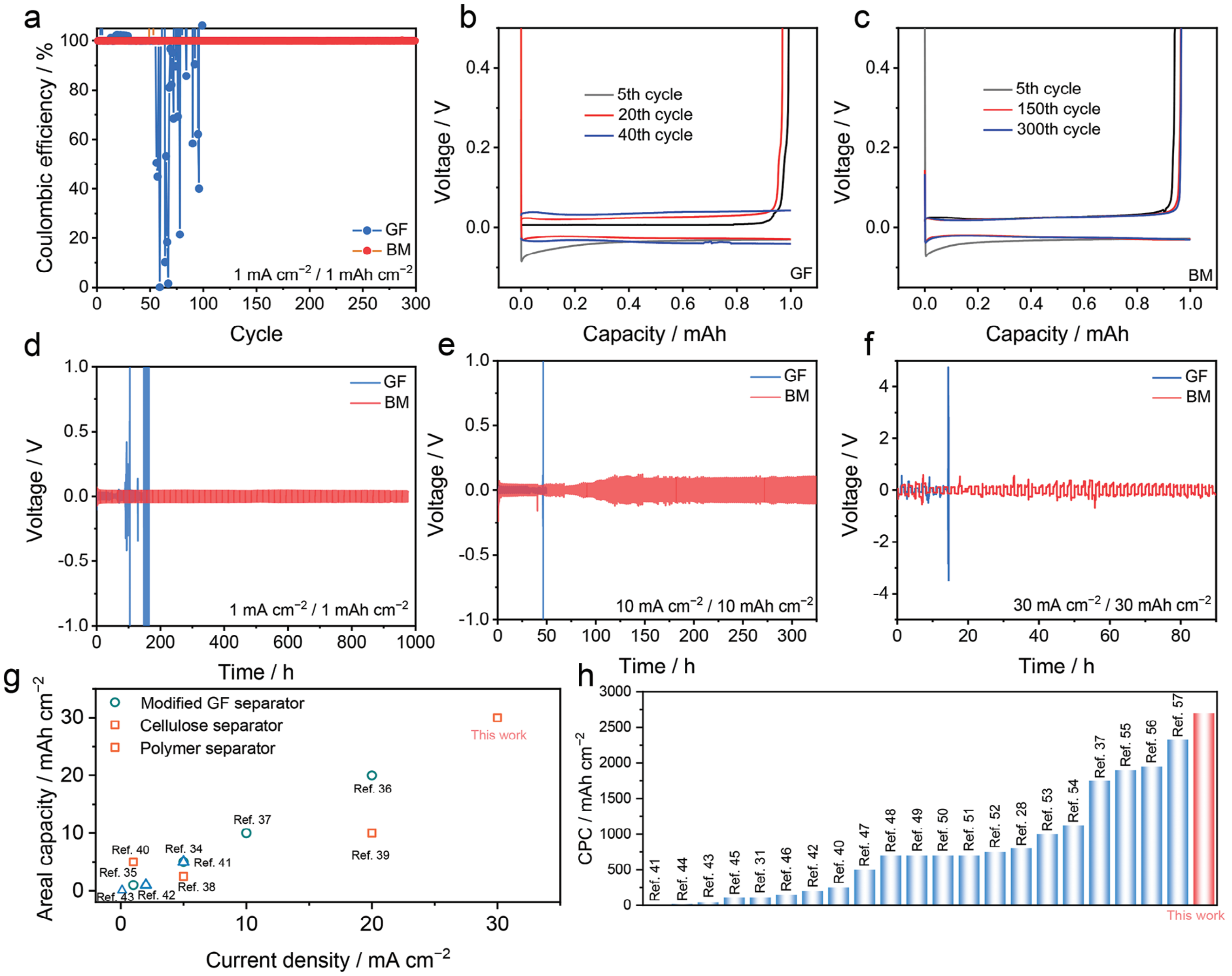

Figure 3. a) CE measurements of Zn/Cu cells using GF and BM separators. Selected GCD curves of Zn/Cu cells using b) GF and c) BM separators. Zn/Zn cells using GF and BM separators tested at d) 1 mA cm^{-2} and 1 mAh cm^{-2}, e) 10 mA cm^{-2} and 10 mAh cm^{-2}, and f) 30 mA cm^{-2} and 30 mAh cm^{-2}. g) Comparison of current density and areal capacity of Zn/Zn cell using BM separator with those recently reported Zn anodes stabilized by various separator strategies. h) CPC of Zn/Zn cell using BM separator with other reported Zn anode with modified separators.

growth. When the test condition further intensifies to 10 mA cm^{-2} and 10 mAh cm^{-2}, the Zn/Zn cell using BM can still work for more than 150 cycles, while the Zn/Cu cell using GF can barely work (Figure 3e). Notably, the Zn/Zn cell with BM shows a cycling stability of more than 80 h at an an ultrahigh current density (30 mA cm^{-2}) and capacity (30 mAh cm^{-2}, Figure 3f). To our knowledge, this is the best cycling performance in separator design (Figure 3g).[34–43] Given the variance in test conditions for assessing the cycling stability of symmetric batteries across previous studies, including differences in testing current densities, prescribed capacities per cycle, and total cycle numbers, this study introduces the use of cumulative plated capacity (CPC) as a means to facilitate a more equitable and precise comparison. As illustrated in Figure 3h, our battery achieves an exceptionally high CPC of 2700 mAh cm^{-2} at a current density of 30 mA cm^{-2}, positioning it at the forefront among reported values in the literature.[28,31,37,40–57]

Scanning electron microscopy (SEM) was adopted to investigate the morphology evolution of Zn anode with different separators. As shown in **Figure** 4a and c, an uneven surface can be observed on the Zn anode after 50 cycles with GF at 1 and 1 mAh cm^{-2}. By contrast, a homogeneous surface of Zn anode is obtained when using BM as separator, convincing a dendrite-free plating morphology can be achieved (Figure 4b and d). The sharp morphology difference of Zn anode cycled in different electrolytes is further demonstrated by laser confocal scanning microscopy. The 3D confocal image of the Zn anode with GF shows agglomerate-like dendrites with high roughness (Figure 4e). With the use of BM, the surface of Zn anode maintains its flat and smooth state (Figure 4f). The XRD patterns of Zn anode after 50 cycles with different separators show similar characteristic peaks as pristine Zn foil, except the ratio of $[002]_{Zn}/[101]_{Zn}$ exposed crystal face increases from 0.66 with GF to 0.87 with BM, suggesting the increased preference of Zn deposits parallel along the zinc

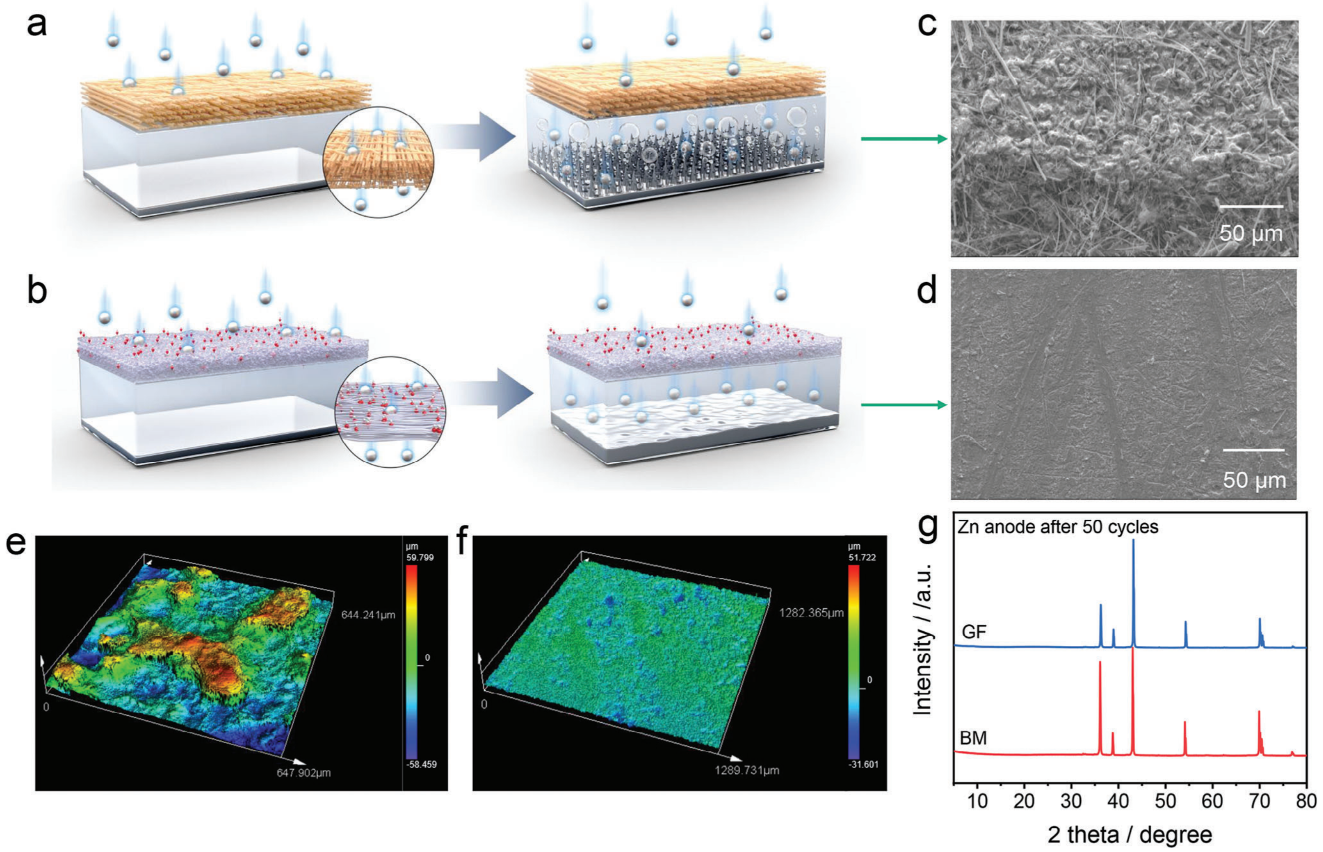

Figure 4. Schematic illustration of Zn deposition process with a) GF and b) BM. SEM images of Zn anode after 50 cycles at 1 and 1 mAh cm^{-2} with c) GF and d) BM. LSCM images of Zn anode after 50 cycles at 1 and 1 mAh cm^{-2} with e) GF and f) BM. g) XRD patterns of Zn anode after 50 cycles at 1 and 1 mAh cm^{-2} using different separators.

anode surface, which is in good agreement with the SEM results (Figure 4g). Moreover, only the Zn anode with GF displays peak representing $Zn_x(OTf)_y(OH)_{2x-y}\cdot H_2O$ by-product, indicating the side reactions can be also suppressed using BM (Figure S14, Supporting Information).

A full cell was assembled to evaluate the feasibility of BM in practical application. $NaV_3O_8\cdot 1.5H_2O$ (NVO) is selected as cathode material due to its high capacity. The successful preparation of NVO is characterized by XRD and SEM (Figure S15, Supporting Information). The cyclic voltammetry (CV) curves of Zn/NVO cells using BM and GF are presented in **Figure 5**a, in which similar redox peaks is observed for both cells, indicating the semblable energy storage mechanism of NVO cathode in both electrolytes. The polarization of redox peaks of Zn/NVO cell using the BM separator is smaller than that using the GF separator, indicating the boosted reaction kinetics of Zn/NVO cell with the BM separator. The rate capability of both cells is tested by GCD, of which capacity retention of 28.1% and 37.6% is obtained for Zn/NVO with GF and BM, respectively, indicating the BM separator has a positive impact on energy storage of Zn/NVO full cell at high rate due to its enhanced interaction with H_2O that facilitate the desolvation process of Zn^{2+} (Figure 5b; Figure S16, Supporting Information). Electrochemical impedance spectroscopy (EIS) of both cells dispalys semicircles in the high-frequency region and linear trajectories in the low-frequency region, indicative of charge-transfer resistance (R_{ct}) and Warburg impedance (R_w), respectively (Figure 5c). The cell using BM demonstrates reduced R_{ct} and R_w in comparison to its counterpart, signifying the enhanced electron and ionic transfer capability of the full cell. This enhancement positively influences the rate performance at elevated current densities, as indicated in Figure 5b. Figure 5d shows the cycling stability of Zn/NVO full cell with GF and BM at a current density of 10 A g^{-1}. For the cell using GF, a rapid capacity decay occurs at ≈380th cycle. By contrast, high capacity retention of 89.7% with near-unity CE is achieved by Zn/NVO cell with BM, confirming the advantages of BM for restraining the activity of water molecules. Furthermore, we assemble two Zn/NVO pouch cells to power the LED lights, indicating the practical ability of the BM separator (Figure 5e).

Furthermore, the primary composite of the BM separator is cellulose, which can be biodegradable therefore allowing it to be effortlessly biodegraded by natural processes after its recycling and reuse. The BM separator can be converted into plant nutrients through the action of bacteria and microorganisms once it is interred in soil. To substantiate the practicality of this degradation pathway, a segment of the BM separator was buried in soil, and its decomposition is monitored over various intervals. As illustrated in **Figure 6**b–e, decomposition began after 3 days, and by 30 days, it had nearly completed. We then placed the BM

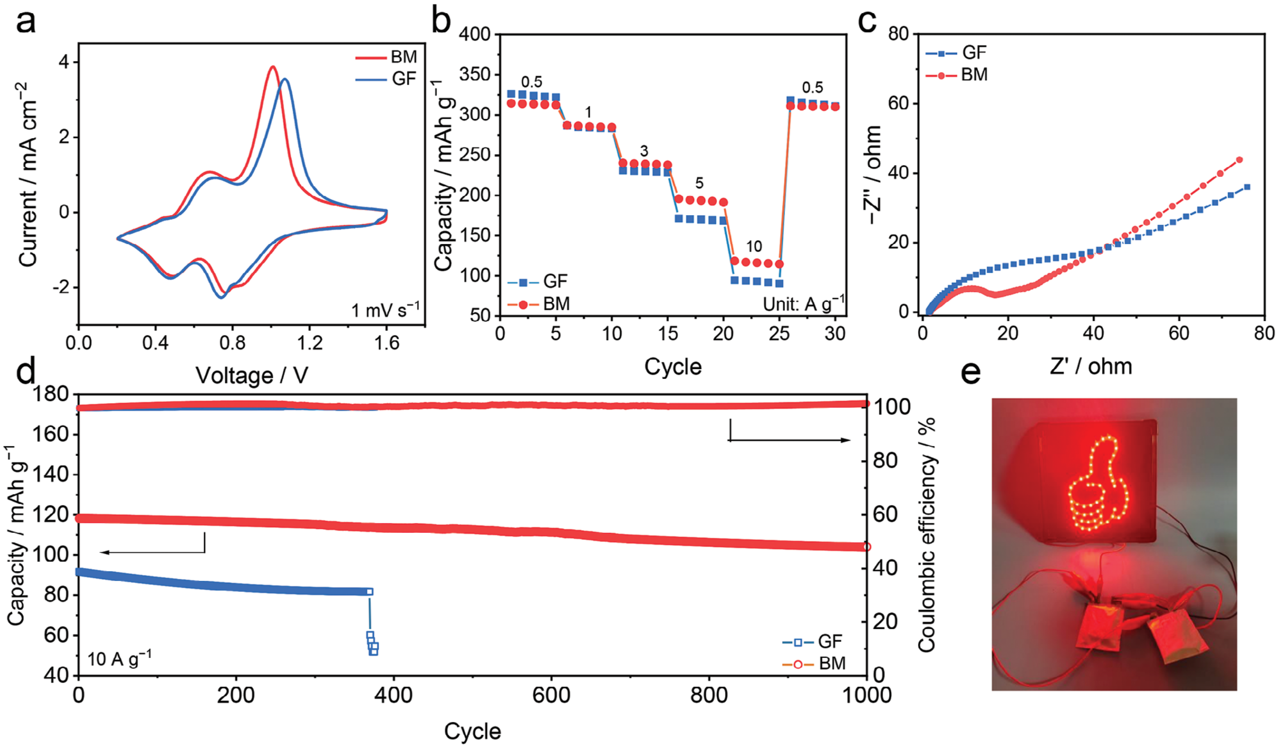

Figure 5. a) CV curevs at 1 mV s^{-1}, b) rate capability, c) EIS, and d) cycling stability at 10 A g^{-1} of Zn/NVO cells using GF and BM separators. e) Photographs of LEDs powered by two Zn/NVO pouch cells.

separator in a *Bacillus* culture fluid and kept at a constant temperature and humidity.[58] After 3 days, microscope images revealed the progression of bacteria colonization on the surface of the BM separator. As the incubation extended, the BM separator was efficiently broken down and assimilated by *Bacillus* species, with the derived nutrients facilitating their proliferation on the separator surface (Figure 6f–i). Overall, the decomposition rate of this eco-friendly, microbially degradable barrier demonstrates commendable efficiency when compared to traditional GF separators.

3. Conclusion

Here, we presented a novel biomass bamboo membrane (BM) separator with high recyclability to inhibit the activity of water molecules in AZIBs, providing an eco-friendly alternative to traditional glass fiber (GF) separators. By attaching oxygen functional groups to the BM separator, it can effectively capture water molecules through hydrogen bonds, transforming their state from free to bound. As a result, the Zn/Zn symmetric cell equipped with this BM separator achieves remarkable performance, operating at an ultrahigh rate and capacity of 30 mA cm^{-2} and 30 mAh cm^{-2} for over 80 h, maintaining a near-perfect CE of ≈99%. In contrast, Zn/Zn cells using GF separators show significantly poorer performance. Furthermore, Zn/NVO full cell utilizing BM separator exhibits 89.7% capacity retention after 1000 cycles at a high current density of 10 A g^{-1}, underscoring the potential of BM separator for enhancing the sustainability and efficiency of AZIBs.

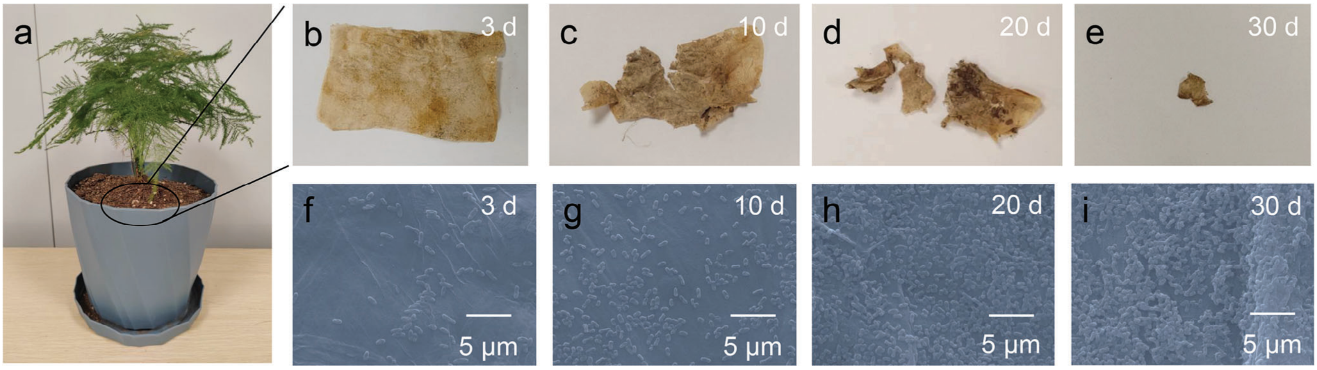

Figure 6. a) Photograph of a pot of green plants of which BM is buried in its soil. Photographs of BM buried in soli after b) 3, c) 10, d) 20 and e) 30 days. f–i) SEM images of *Bacillus* on the BM at different stages of decomposition.

Supporting Information

Supporting Information is available from the Wiley Online Library or from the author.

Acknowledgements

The authors are grateful for grants from the National Key R&D Program of China (2022YFD2200904).

Conflict of Interest

The authors declare no conflict of interest.

Data Availability Statement

The data that support the findings of this study are available from the corresponding author upon reasonable request.

Keywords

aqueous Zn ion batteries, bamboo membrane, high-capacity, separator, Zn anode

Received: May 5, 2024
Revised: July 4, 2024
Published online: September 10, 2024

[1] X. Yu, Z. Li, X. Wu, H. Zhang, Q. Zhao, H. Liang, H. Wang, D. Chao, F. Wang, Y. Qiao, H. Zhou, S. G. Sun, *Joule* **2023**, *7*, 1145.
[2] J. Cao, D. Zhang, X. Zhang, Z. Zeng, J. Qin, Y. Huang, *Energy Environ. Sci.* **2022**, *15*, 499.
[3] Z. Zhang, X. Yang, P. Li, Y. Wang, X. Zhao, J. Safaei, H. Tian, D. Zhou, B. Li, F. Kang, G. Wang, *Adv. Mater.* **2022**, *34*, 2206970.
[4] X. Zeng, K. Xie, S. Liu, S. Zhang, J. Hao, J. Liu, W. K. Pang, J. Liu, P. Rao, Q. Wang, J. Mao, Z. Guo, *Energy Environ. Sci.* **2021**, *14*, 5947.
[5] L. Ma, M. A. Schroeder, O. Borodin, T. P. Pollard, M. S. Ding, C. Wang, K. Xu, *Nat. Energy* **2020**, *5*, 743.
[6] J. Zheng, Q. Zhao, T. Tang, J. Yin, C. D. Quilty, G. D. Renderos, X. Liu, Y. Deng, L. Wang, D. C. Bock, C. Jaye, D. Zhang, E. S. Takeuchi, K. J. Takeuchi, A. C. Marschilok, L. A. Archer, *Science* **2019**, *366*, 645.
[7] N. Zhang, S. Huang, Z. Yuan, J. Zhu, Z. Zhao, Z. Niu, *Angew. Chem., Int. Ed.* **2021**, *60*, 2861.
[8] P. Zou, R. Zhang, L. Yao, J. Qin, K. Kisslinger, H. Zhuang, H. L. Xin, *Adv. Energy Mater.* **2021**, *11*, 2100982.
[9] Y. Mu, Z. Li, B. Wu, H. Huang, F. Wu, Y. Chu, L. Zou, M. Yang, J. He, L. Ye, M. Han, T. Zhao, L. Zeng, *Nat. Commun.* **2023**, *14*, 4205.
[10] X. Shi, J. Wang, F. Yang, X. Liu, Y. Yu, X. Lu, *Adv. Funct. Mater.* **2023**, *33*, 2211917.
[11] F. Ming, Y. Zhu, G. Huang, A.-H. Emwas, H. Liang, Y. Cui, H. N. Alshareef, *J. Am. Chem. Soc.* **2022**, *144*, 7160.
[12] X. Shi, J. Xie, J. Wang, S. Xie, Z. Yang, X. Lu, *Nat. Commun.* **2024**, *15*, 302.
[13] X. Yang, Z. Zhang, M. Wu, Z. Guo, Z. Zheng, *Adv. Mater.* **2023**, *35*, 2303550.
[14] W. Xu, J. Li, X. Liao, L. Zhang, X. Zhang, C. Liu, K. Amine, K. Zhao, J. Lu, *J. Am. Chem. Soc.* **2023**, *145*, 22456.
[15] Q. Zhang, Y. Ma, Y. Lu, X. Zhou, L. Lin, L. Li, Z. Yan, Q. Zhao, K. Zhang, J. Chen, *Angew. Chem., Int. Ed.* **2021**, *133*, 23545.
[16] F. Yang, J. A. Yuwono, J. Hao, J. Long, L. Yuan, Y. Wang, S. Liu, Y. Fan, S. Zhao, K. Davey, Z. Guo, *Adv. Mater.* **2022**, *34*, 2206754.
[17] L. Zhou, F. Wang, F. Yang, X. Liu, Y. Yu, D. Zheng, X. Lu, *Angew. Chem., Int. Ed.* **2022**, *134*, 202208051.
[18] Y. Zeng, X. Zhang, R. Qin, X. Liu, P. Fang, D. Zheng, Y. Tong, X. Lu, *Adv. Mater.* **2019**, *31*, 1903675.
[19] H. Ren, S. Li, B. Wang, Y. Zhang, T. Wang, Q. Lv, X. Zhang, L. Wang, X. Han, F. Jin, C. Bao, P. Yan, N. Zhang, D. Wang, T. Cheng, H. Liu, S. Dou, *Adv. Mater.* **2023**, *35*, 2208237.
[20] X. Luan, L. Qi, Z. Zheng, Y. Gao, Y. Xue, Y. Li, *Angew. Chem., Int. Ed.* **2023**, *62*, 202215968.
[21] F. Wang, O. Borodin, T. Gao, X. Fan, W. Sun, F. Han, A. Faraone, J. A. Dura, K. Xu, C. Wang, *Nat. Mater.* **2018**, *17*, 543.
[22] L. Cao, D. Li, E. Hu, J. Xu, T. Deng, L. Ma, Y. Wang, X.-Q. Yang, C. Wang, *J. Am. Chem. Soc.* **2020**, *142*, 21404.
[23] R. Qin, Y. Wang, M. Zhang, Y. Wang, S. Ding, A. Song, H. Yi, L. Yang, Y. Song, Y. Cui, J. Liu, Z. Wang, S. Li, Q. Zhao, F. Pan, *Nano Energy* **2021**, *80*, 105478.
[24] S. Liu, J. Mao, W. K. Pang, J. Vongsvivut, X. Zeng, L. Thomsen, Y. Wang, J. Liu, D. Li, Z. Guo, *Adv. Funct. Mater.* **2021**, *31*, 2104281.
[25] H. Yang, Z. Chang, Y. Qiao, H. Deng, X. Mu, P. He, H. Zhou, *Angew. Chem., Int. Ed.* **2020**, *59*, 9377.
[26] L. Ma, Q. Li, Y. Ying, F. Ma, S. Chen, Y. Li, H. Huang, C. Zhi, *Adv. Mater.* **2021**, *33*, 2007406.
[27] Y. Zong, H. He, Y. Wang, M. Wu, X. Ren, Z. Bai, N. Wang, X. Ning, S. X. Dou, *Adv. Energy Mater.* **2023**, *13*, 2300403.
[28] W. Zhou, M. Chen, Q. Tian, J. Chen, X. Xu, C.-P. Wong, *Energy Storage Mater.* **2022**, *44*, 57.
[29] L. Li, S. Jia, Z. Cheng, C. Zhang, *ChemSusChem* **2023**, *16*, 202202330.
[30] J. Mei, X. Peng, Q. Zhang, X. Zhang, T. Liao, V. Mitic, Z. Sun, *Adv. Funct. Mater.* **2021**, *31*, 2100299.
[31] Y. Fang, X. Xie, B. Zhang, Y. Chai, B. Lu, M. Liu, J. Zhou, S. Liang, *Adv. Funct. Mater.* **2022**, *32*, 2109671.
[32] X. Xie, S. Liang, J. Gao, S. Guo, J. Guo, C. Wang, G. Xu, X. Wu, G. Chen, J. Zhou, *Energy Environ. Sci.* **2020**, *13*, 503.
[33] T. Ma, Y. Ni, Q. Wang, W. Zhang, S. Jin, S. Zheng, X. Yang, Y. Hou, Z. Tao, J. Chen, *Angew. Chem., Int. Ed.* **2022**, *134*, 202207927.
[34] C. Li, Z. Sun, T. Yang, L. Yu, N. Wei, Z. Tian, J. Cai, J. Lv, Y. Shao, M. H. Rümmeli, J. Sun, Z. Liu, *Adv. Mater.* **2020**, *32*, 2003425.
[35] Y. Guo, W. Cai, Y. Lin, Y. Zhang, S. Luo, K. Huang, H. Wu, Y. Zhang, *Energy Storage Mater.* **2022**, *50*, 580.
[36] J. Cao, D. Zhang, X. Zhang, M. Sawangphruk, J. Qin, R. Liu, *J. Mater. Chem. A* **2020**, *8*, 9331.
[37] Z. Hou, Y. Gao, H. Tan, B. Zhang, *Nat. Commun.* **2021**, *12*, 3083.
[38] J. Cao, D. Zhang, C. Gu, X. Zhang, M. Okhawilai, S. Wang, J. Han, J. Qin, Y. Huang, *Nano Energy* **2021**, *89*, 106322.
[39] J. Cao, D. Zhang, C. Gu, X. Wang, S. Wang, X. Zhang, J. Qin, Z. Wu, *Adv. Energy Mater.* **2021**, *11*, 2101299.
[40] X. Ge, W. Zhang, F. Song, B. Xie, J. Li, J. Wang, X. Wang, J. Zhao, G. Cui, *Adv. Funct. Mater.* **2022**, *32*, 2200429.
[41] M. Ghosh, V. Vijayakumar, S. Kurungot, *Energy Technol.* **2019**, *7*, 1900442.
[42] Y. Liu, S. Liu, X. Xie, Z. Li, P. Wang, B. Lu, S. Liang, Y. Tang, J. Zhou, *InfoMat* **2023**, *5*, 12374.
[43] J. Li, Y. Chen, J. Guo, F. Wang, H. Liu, Y. Li, *Adv. Funct. Mate.* **2020**, *30*, 2004115.
[44] N. Maeboonruan, J. Lohitkarn, C. Poochai, T. Lomas, A. Wisitsoraat, S. Kheawhom, S. Siwamogsatham, A. Tuantranont, C. Sriprachuabwong, *J. Sci.: Adv. Mater. Devices* **2022**, *7*, 100467.
[45] D. Yuan, W. Manalastas, L. Zhang, J. J. Chan, S. Meng, Y. Chen, M. Srinivasan, *ChemSusChem* **2019**, *12*, 4889.
[46] L. Li, J. Peng, X. Jia, X. Zhu, B. Meng, K. Yang, D. Chu, N. Yang, J. Yu, *Electrochim. Acta* **2022**, *430*, 141129.

[47] Z. Wang, L. Dong, W. Huang, H. Jia, Q. Zhao, Y. Wang, B. Fei, F. Pan, *Nano-Micro Lett.* **2021**, *13*, 73.

[48] L. Wu, Y. Zhang, P. Shang, Y. Dong, Z.-S. Wu, *J. Mater. Chem. A* **2021**, *9*, 27408.

[49] H. Yang, Y. Qiao, Z. Chang, H. Deng, P. He, H. Zhou, *Adv. Mater.* **2020**, *32*, 2004240.

[50] X. Yang, W. Wu, Y. Liu, Z. Lin, X. Sun, *Chem. Eng. J.* **2022**, *450*, 137902.

[51] P. Cao, H. Zhou, X. Zhou, Q. Du, J. Tang, J. Yang, *ACS Sustainable Chem. Eng.* **2022**, *10*, 8350.

[52] L. Tan, Y. Sun, C. Wei, Y. Tao, Y. Tian, Y. An, Y. Zhang, S. Xiong, J. Feng, *Small* **2021**, *17*, 2007717.

[53] Y. Zhang, X. Li, L. Fan, Y. Shuai, N. Zhang, *Cell Rep. Phys. Sci.* **2022**, *3*, 100824.

[54] X. Zhang, S. Yang, Z. Huang, Z. Zeng, Y. Zhang, Z. Wang, *Electrochim. Acta* **2022**, *430*, 141081.

[55] X. Yang, W. Li, J. Lv, G. Sun, Z. Shi, Y. Su, X. Lian, Y. Shao, A. Zhi, X. Tian, X. Bai, Z. Liu, J. Sun, *Nano Res.* **2022**, *15*, 9785.

[56] Y. Qin, P. Liu, Q. Zhang, Q. Wang, D. Sun, Y. Tang, Y. Ren, H. Wang, *Small* **2020**, *16*, 2003106.

[57] C. Peng, Y. Zhang, S. Yang, L.-L. Zhang, Z. Wang, *Nano Energy* **2022**, *98*, 107329.

[58] H. Lu, J. Hu, X. Wei, K. Zhang, X. Xiao, J. Zhao, Q. Hu, J. Yu, G. Zhou, B. Xu, *Nat. Commun.* **2023**, *14*, 4435.